JMI Journal of Medical Imaging

RESEARCH PAPER

Spectral optimization using fast kV switching and filtration for photon counting CT with realistic detector responses: a simulation study

Sen Wang[a,*] Yirong Yang,[a,b] Debashish Pal,[c] Zhye Yin,[c] Jonathan S. Maltz,[c,d] Norbert J. Pelc[a] and Adam S. Wang[a,b]

[a]Stanford University, Department of Radiology, Stanford, California, United States
[b]Stanford University, Department of Electrical Engineering, Stanford, California, United States
[c]GE HealthCare, Waukesha, Wisconsin, United States
[d]Molecular Biophysics and Integrated Bioimaging, Lawrence Berkeley National Laboratory, Berkeley, California, United States

ABSTRACT. **Purpose:** Photon counting CT (PCCT) provides spectral measurements for material decomposition. However, the image noise (at a fixed dose) depends on the source spectrum. Our study investigates the potential benefits from spectral optimization using fast kV switching and filtration to reduce noise in material decomposition.

Approach: The effect of the input spectra on noise performance in both two-basis material decomposition and three-basis material decomposition was compared using Cramer-Rao lower bound analysis in the projection domain and in a digital phantom study in the image domain. The fluences of different spectra were normalized using the CT dose index to maintain constant dose levels. Four detector response models based on Si or CdTe were included in the analysis.

Results: For single kV scans, kV selection can be optimized based on the imaging task and object size. Furthermore, our results suggest that noise in material decomposition can be substantially reduced with fast kV switching. For two-material decomposition, fast kV switching reduces the standard deviation (SD) by ~10%. For three-material decomposition, greater noise reduction in material images was found with fast kV switching (26.2% for calcium and 25.8% for iodine, in terms of SD), which suggests that challenging tasks benefit more from the richer spectral information provided by fast kV switching.

Conclusions: The performance of PCCT in material decomposition can be improved by optimizing source spectrum settings. Task-specific tube voltages can be selected for single kV scans. Also, our results demonstrate that utilizing fast kV switching can substantially reduce the noise in material decomposition for both two- and three-material decompositions, and a fixed Gd filter can further enhance such improvements for two-material decomposition.

 [DOI: 10.1117/1.JMI.11.S1.S12805]

Keywords: photon counting detectors; material decomposition; spectral optimization; fast kV switching

Paper 23092GRRR received Apr. 14, 2023; revised May 16, 2024; accepted Jul. 8, 2024; published Jul. 25, 2024.

1 Introduction

Spectral CT with basis material imaging was first proposed by Alvarez and Macovski[1] and exploited two spectral measurements to provide material-specific images. More recently,

*Address all correspondence to Sen Wang, senwang@stanford.edu

2329-4302/2024/$28.00

dual-energy CT systems have become commonplace and can be divided into four categories: dual source,[2] fast kV switching,[3] slow kV switching,[4] and dual-layer detector.[5]

The basic principle behind material decomposition relates to the interaction between x-ray photons and matter, which can be utilized to quantify basis materials and to generate virtual noncontrast images, iodine maps, and virtual monoenergetic images (VMIs).[6] These features of material decomposition provide distinct advantages in various clinical situations. For instance, material decomposition has shown potential in improving the diagnostic accuracy of acute bowel ischemia[7] and facilitating the detection of pulmonary emboli,[8] leveraging iodine contrast and VMIs. Virtual noncontrast images from material decomposition have also demonstrated utility in detecting adrenal adenomas[9] and fatty liver.[10] The increased material differentiation provides benefits in brain hemorrhage identification,[11–13] renal lesion characterization,[14] and calcification diagnosis.[15]

Conventional dual-energy CT systems use energy-integrating detectors (EIDs), which lose the spectral information of photons and add electronic noise as well as Swank noise, thus limiting the overall image quality in terms of noise and image contrast.[16] Photon counting detectors (PCDs), however, count incoming photons individually and measure the energy of each. By setting the lowest threshold above the electronic noise floor, it is possible to minimize the negative impact of electronic noise. Advantages of PCDs, such as increased signal-to-noise ratio,[17] better image resolution,[18–20] and improved low-dose performance,[21] have been widely studied over the past several years. As the fabrication of large-area detectors recently became feasible and cost-effective, vendors are constructing photon-counting CT (PCCT) systems based on CdTe/CZT and Si PCDs.[22,23]

However, PCDs are not flawless, and their performance is reduced by various nonideal factors, such as charge sharing, K-escape, and pulse pileup. These degrade the overall performance, leading to increased noise in material decomposition. To compensate for the degradation caused by the nonideal detector response in PCDs, this study investigates the potential benefits of spectral optimization with realistic detector responses.

The concept of spectral optimization was previously explored in dual-energy CT to reduce noise and/or improve dose efficiency in material decomposition tasks. As the noise performance of dual-energy CT depends on the energy separation between the two spectral measurements, combinations of kV pairs, such as 80/140 and 100/140 kV, were investigated as well as different filtration strategies: an Sn filter for high kV in dual-source systems[24,25] and a fixed K-edge filter (Gd) in fast kV switching systems.[26] The efficacy of these methods was evaluated in experiments on EID systems.

For PCDs, spectral optimization techniques include a fixed K-edge filter,[27] task-oriented tube voltage optimization for single-kV systems,[28,29] and dual-spectra acquisition for dual-source systems.[30,31] Compared to dual-source systems, fast kV switching possesses distinct properties. It generates high-kV and low-kV measurements that are closely aligned in the projection domain, from a single source–detector pair. The work we present here is aimed at PCDs with fast kV switching. Preliminary work was presented in our conference paper.[32] The two contributions of this study are as follows.

(a) Fast kV switching is a realization of dual spectrum acquisition that can provide additional spectral information using a single source. We evaluate its potential supplemental benefits through a simulation study. Additionally, we show that a fixed Gd filter or high kV-only filter improves two-material decomposition.

(b) We find the relative benefit of spectral optimization to be even higher for the case of three-basis material decomposition (water + Ca + iodine) versus the case of two basis materials (water + Ca).

2 Materials and Methods

2.1 Material Decomposition and CRLB Analysis

In the diagnostic energy range, material attenuation coefficients can be decomposed into a linear combination of basis materials:

$$\mu(E) = \sum_{i=1}^{M} \alpha_i f_i(E), \tag{1}$$

where α_i is the decomposition coefficient, $f_i(E)$ is the mass attenuation of the i'th basis material as a function of energy E, and M denotes the number of basis materials. If there are no K-edges, no more than two basis materials can be separated, and $M = 2$. K-edge materials can be added as further basis materials.

The material decomposition method estimates the line integral of decomposition coefficients when spectral measurements are available. The expected spectral measurements of PCDs can be formulated as

$$\lambda_j^{(\mathrm{kV})} = \int_{\mathrm{bin}_j} \mathrm{d}E' \int_0^{E_{\max}} \mathrm{d}E \cdot S^{(\mathrm{kV})}(E;\mathrm{filter}) \exp\left(-\sum_{i=1}^{M} A_i f_i(E)\right) h(E';E), \tag{2}$$

where $\lambda_j^{(\mathrm{kV})}$ are the detected photon counts in the j'th energy bin, $S^{(\mathrm{kV})}(E;\mathrm{filter})$ is the filtered source spectrum at tube voltage kV, $A_i = \int_l \alpha_i(\boldsymbol{r})\mathrm{d}l$ are line integrals through the object represented by spatial distributions of $\alpha_i(\boldsymbol{r})$, and $h(E';E)$ is the detector response, which models the nonideal response and probability that a photon of energy E is detected at energy E'.

To perform material decomposition, the basis material line integrals A_i must be estimated from binned counts $\gamma_j \sim \mathrm{Poisson}(\lambda_j)$. The Cramér–Rao lower bound (CRLB) is widely used in estimating the achievable noise level of material decomposition[33] (in terms of variance) since it predicts the minimum variance of an unbiased estimator. For single kV scans, the CRLB can be calculated directly given the source spectrum, detector response, and basis materials. In addition, we explored the potential of fast kV switching in PCCT systems. Fast kV switching uses a single x-ray tube to rapidly alternate between low and high kV levels, so there is minimal rotation between the projections (for simplicity, we assume adjacent projections [energy pairs] are spatially aligned). Hence, we assume that fast kV switching leads to independent PCD measurements of the object with different spectra that the maximum likelihood estimator (MLE) can take advantage of. The CRLB calculation when fast kV switching is applied is as follows:

$$F_{m,n} = -E\left(\frac{\partial^2 L(\boldsymbol{\gamma}|\boldsymbol{A})}{\partial A_m \partial A_n}\right) = \sum_{\mathrm{kV}} \sum_{j=1}^{N} \frac{1}{\lambda_j^{(\mathrm{kV})}} \frac{\partial \lambda_j^{(\mathrm{kV})}}{\partial A_m} \frac{\partial \lambda_j^{(\mathrm{kV})}}{\partial A_n}, \tag{3}$$

$$L(\boldsymbol{\gamma}|\boldsymbol{A}) = \sum_{\mathrm{kV}} \sum_{j=1}^{N} (\lambda_j(\boldsymbol{A}) - \gamma_j \ln \lambda_j(\boldsymbol{A})), \tag{4}$$

$$\mathrm{CRLB}_{A_i} = \{F^{-1}\}_{i,i}, \tag{5}$$

where $F_{m,n}$ are elements of the Fisher information matrix, and $L(\boldsymbol{\gamma}|\boldsymbol{A})$ denotes the log-likelihood of the measurements $\boldsymbol{\gamma}$ (photon counts in N energy bins for PCDs). In comparison to the commonly used CRLB equation, Eqs. (3) and (4) contain an additional summation over different kV values to accommodate independent measurements obtained for each source spectrum. Finally, taking the inverse of the Fisher information matrix yields the CRLB.

VMIs are also of importance in clinical practice. We analyzed their variance properties in addition to those of the material images. The VMI at a specified energy E represents the material attenuation at the corresponding energy as Eq. (1) shows. Its CRLB can be obtained analytically from the CRLB of basis materials:

$$\mathrm{CRLB}_{\mathrm{VMI}(E)} = f^{\mathrm{T}}(E) F^{-1} f(E), \tag{6}$$

where $f(E) = [f_1(E), \ldots, f_M(E)]^{\mathrm{T}}$ are the basis material mass attenuation coefficients and F is the Fisher information matrix. In this study, VMIs were generated in the range 40 to 120 keV, with an increment of 10 keV.

2.2 Simulation Settings and Detector Responses in This Study

To study realistic performance, we used the detector responses from Monte Carlo simulations that were reported in separate work,[31] choosing four representative detector designs of sensor

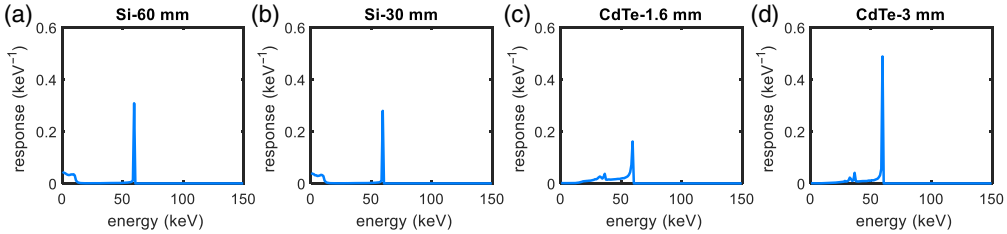

Fig. 1 Detector responses. The blue curve denotes the detector response at 60 keV for all the detectors, where the detection efficiencies are (a) 0.80 (Si-60 mm), (b) 0.72 (Si-30 mm), (c) 0.99 (CdTe-1.6 mm), and (d) 0.99 (CdTe-3 mm).

materials and depths: Si-60 mm (pixel size: 0.5×0.5 mm^2), Si-30 mm (pixel size: 0.5×0.5 mm^2), CdTe-1.6 mm (pixel size: 0.225×0.225 mm^2), and CdTe-3 mm (pixel size: 0.5×0.5 mm^2). In the silicon detectors, 20 μm tungsten foils are added between silicon wafers to reduce crosstalk between detector pixel rows. For simplicity, we use the detectors' primary responses, without modeling object scatter, pixel-to-pixel crosstalk arising from Compton scatter, K-fluorescence, and charge sharing or pulse pileup. Figure 1 shows the responses of these detectors when irradiated with 60 keV photons, where detection efficiencies are the fraction of incident photons that are detected above the lowest threshold. (Spectral performance depends on both detection efficiency and spectral response.)

In this study, basis material attenuation and source spectra were obtained from CatSim (GE Research, Niskayuna, New York), where the source spectra represent those of the GE Revolution CT system (GE HealthCare, Waukesha, Wisconsin).[34] For the single kV comparison, we evaluated 80/100/120/140 kV spectra. For fast kV switching, we focused on the 80/140 kV combination that is commonly employed on contemporary clinical systems.[35] In terms of potential filters, rapid mechanical switching of a filter at the electronic kV switching rate [several kHz] is a practical challenge, so we primarily assumed that the filters are uniformly applied to both low and high kV spectra. However, the tube current needs to be increased when a filter is applied to compensate for the intensity reduction, which may be challenging for the source. Therefore, in our study, we limited the intensity reduction for the 80 kV spectrum to be less than 50%. Specifically, two different filters (Sn-0.07 mm, Gd-0.09 mm) were evaluated as potential absorbers. In addition, with the aim of fully exploring the potential of spectral optimization, we also incorporated the simulation of a dedicated Sn-0.4 mm filter for the 140 kV spectrum only.[30,31] This could be realized either through a fast kV switching system, if rapid filter switching is possible, or through sequential scans or a dual-source system, if appropriate registration of projection domain measurements can be achieved.

In our study, water and calcium were selected as the basis materials for two-material decomposition, and iodine (K-edge at 33.2 keV) was added as a third basis material for three-material decomposition. The eight energy thresholds of the detector were set at 15, 27, 34, 40, 45, 54, 63, and 76 keV for the Si detector, in order to minimize the average CRLB for water from 0 to 40 cm and cortical bone from 0 to 5 cm.[36,37] Contemporary CdTe-based detectors typically provide fewer than eight energy bins,[38] but this is a design choice rather than a limitation. Consequently, for consistency in our study, we assume all detectors utilize the same number of bins and set the lowest threshold of the CdTe detector to be 25 keV for finding the optimal thresholds (25, 39, 47, 53, 61, 70, 80, and 95 keV).

2.3 Dose Normalization

To ensure equal dose in all scenarios, a fast Monte Carlo tool[39] for CTDI estimation was applied for all combinations of kV and filtration in order to obtain corresponding dose normalization factors. This tool was adapted from MC-GPU[40] and is capable of calculating dose with realistic CT system models that includes a nonisotropic source due to anode heel effect and bowtie filtration.

MC-GPU outputs dose in units of eV/g per photon. Table 1 summarizes the dose contribution from each photon (denoted as η) to CTDI values of the 32 cm body phantom used for dose normalization. Furthermore, the clinical relevance of η to CTDI values can be understood by

Table 1 Dose normalization factors with respect to 120 kV scan without a filter (where the equivalent dose exposure is normalized to 1.00).

Source settings			
Tube voltage	Filter	η (eV/g per photon)	Equivalent dose exposure (mAs)
80 kV	No filter	0.88	3.17
	Gd-0.09 mm	0.45	8.89
	Sn-0.07 mm	0.48	8.42
100 kV	No filter	1.00	1.64
	Gd-0.09 mm	0.54	3.04
	Sn-0.07 mm	0.63	2.61
120 kV	No filter	1.12	**1.00**
	Gd-0.09 mm	0.64	1.74
	Sn-0.07 mm	0.77	1.45
140 kV	No filter	1.23	0.67
	Gd-0.09 mm	0.75	1.09
	Sn-0.07 mm	0.90	0.91
	Sn-0.40 mm	0.36	2.25

considering the photon fluence per mAs at different kV's. To demonstrate it, we listed the equivalent-dose exposure in terms of mAs under different source settings in Table 1, normalized to 120 kV without filter. For example, an exposure of 3.17 mAs at 80 kV produces an equivalent dose to an exposure of 1.00 mAs at 120 kV, both without filter. Plots of the dose-normalized spectra are shown in Fig. 2. In the simulation, the 120 kV spectrum without filter functioned as the reference, and the intensities of the other spectra (at different kV's or with different filters) were scaled based on the ratio in Table 1. In all simulation tasks, $\Phi_{120\,\mathrm{kV}}$ was set to 4×10^6 photons/mm^2 at the detector for an air scan condition.

2.4 Numerical Study Across Projection Domain and Image Domain

CRLB analysis focuses on noise properties in the projection domain. It predicts the variance of material decomposition sinograms, prior to reconstruction. In our projection domain analysis, we selected a range of water (0 to 40 cm at 1 g/cm^3) and calcium (0 to 2 cm at 1.55 g/cm^3, or equivalently the calcium in 0 to 7.18 cm cortical bone[37]) to cover all clinically relevant

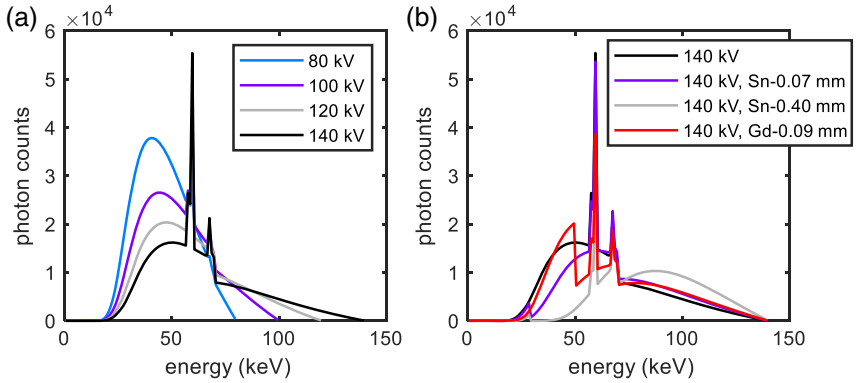

Fig. 2 Dose-normalized spectra: (a) 80/100/120/140 kV spectra at matched dose and (b) 80, 140, 140 kV with Sn-0.07 mm filter, 140 kV with Sn-0.4 mm filter, and 140 kV with Gd-0.09 mm filter at matched dose.

thicknesses. In the comparison between different source settings, the CRLB ratio was calculated to demonstrate the relative noise performance. For three-material decomposition, an iodine solution (0 to 1 cm at 5 mg/mL) was added to the simulation and analysis.

To investigate the impact of dose allocation within the switching pair, we selected a region of interest (ROI) in the central region of the material thicknesses plane (water: 10 to 30 cm and Ca: 0 to 2 cm) and calculated the mean CRLB ratios of basis decomposition and VMIs at 40, 60, and 70 keV in this region as the quantitative metric, which have been used in various clinical applications.[7,41–46]

For image domain analysis, we simulated an axial CT scan of an anthropomorphic head phantom[47] with a typical CT geometry modeled after the GE revolution scanner and the realistic PCD energy responses. Binned counts in the projection domain were simulated using Eq. (2), with Poisson noise added to the expected counts. After MLE decomposition in the projection domain, followed by filtered backprojection reconstruction with a standard kernel used in GE's CT reconstruction,[34] we evaluated noise levels in the image domain. Unlike the CRLB analysis in the projection domain that gives the estimation of variance in the decomposition, we opted to express the noise in the image domain as the standard deviation (SD), which is a more common measure. It can be obtained in the difference images between the noisy and ground truth simulated images.

3 Results

In this section, we first present the results for two-basis material decomposition with the Si-60 mm detector response under single kV and fast kV switching scenarios. Then, we present data for other realistic detector responses as well as the image domain analysis. Finally, we show the noise performance when a K-edge material (iodine) is included.

3.1 Optimal Single-kV Scan

We compared the CRLB for 80/100/120/140 kV in single kV scans using 120 kV as a reference when dose was kept constant for the Si-60 mm detector and identified the contours corresponding to a ratio of 1 for each source. Such contours divide the CRLB ratio map into optimal kV subregions for both the water basis and Ca basis, as shown in Fig. 3. Each subregion is labeled with one particular kV value, which indicates the spectrum that yields the lowest noise (smallest CRLB) in that region. In general, we found thicker objects benefit from higher kV, as expected. Additionally, Ca benefits more from lower kV than is the case for water.

3.2 CRLB Analysis in Projection Domain with Fast kV Switching

In this section, we present the CRLB analysis in projection domain when fast kV switching is available, along with the Si-60 mm detector. The impact of dose allocation is shown in Fig. 4 where we plotted the CRLB ratio at different dose allocations. The horizontal axis denotes the dose allocation for 80 kV. The optimal allocation can vary with respect to different tasks and different filters applied. We found a 30/70% allocation between the 80/140 kV spectra provides good performance [Fig. 4(a)] while 40/60% is preferred with a fixed Gd filter [Fig. 4(b)]. We applied this optimization for all source settings.

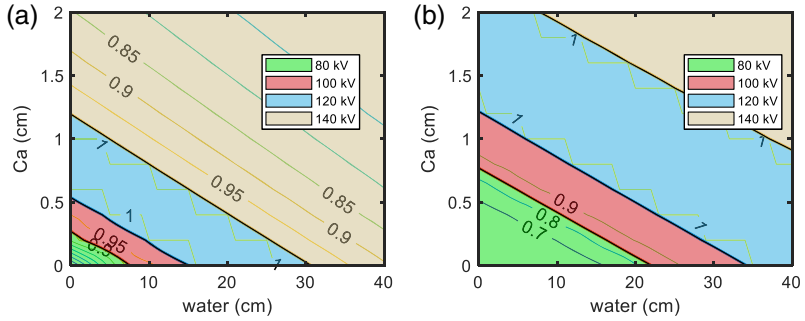

Fig. 3 Optimal kV for a single kV scan, depending on basis material and object thickness for a Si-60 mm detector: (a) water basis and (b) Ca basis.

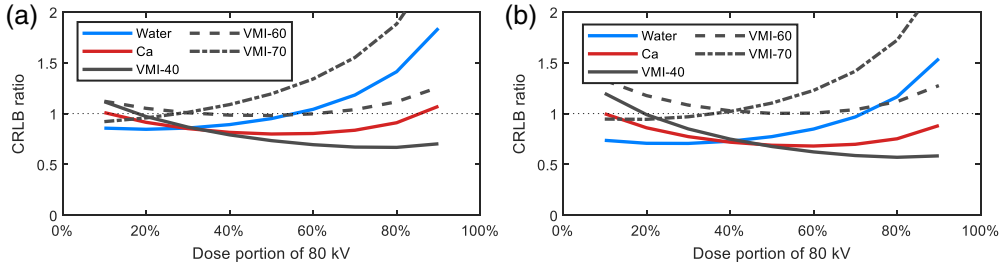

Fig. 4 Dose allocation and CRLB ratios for an ROI of 10 to 30 cm water and 0 to 2 cm Ca. (a) 80/140 switching without additional filters. (b) 80/140 switching pair with fixed Gd-0.09 mm filter. The optimal dose allocation depends on the task and the filter applied to the source.

The maps of CRLB ratios between the 80/140 kV pair with different filters and 120 kV are shown in Fig. 5. The contours having a ratio >1 are highlighted in red for both water and Ca bases. We find a nearly universal improvement in noise performance for both water and Ca decomposition using fast kV switching with or without Gd filter when dose is properly allocated in Figs. 5(b) and 5(c). We believe this is due to improved spectral information from the lower energy spectrum (80 kV) for thinner areas and higher energy spectrum (140 kV) for thicker areas compared with a single spectrum (120 kV).

In contrast, we also include the results from a suboptimal 50/50% dose allocation in Fig. 5(a), which demonstrates that the proper dose allocation [Fig. 5(b)] can effectively suppress the penalty highlighted in red in Fig. 5(a). We can also observe some penalties in fast kV switching with fixed Sn-0.07 mm filter in the thinner area. Because Sn is largely a beam hardening filter, it removes lower energy photons that are important for smaller objects.

Therefore, with proper dose allocation and filter selection, fast kV switching could be used regardless of object size, unlike the optimal single kV, which depends on the object size and task.

The mean CRLB ratios under different source settings are listed in Table 2 with optimal dose allocation selected for the corresponding switching pairs, which contains seven different source settings, in which the first three rows denote single kV (120 kV) with/without filters, and the last four rows denote dual kV scans with/without filters. In Table 2, we observe a consistent improvement from dual kV scans for water and Ca, with some minor penalty for VMIs. The performance of the 80/140 pair for water and calcium tasks can be further enhanced by incorporating a fixed Gd-0.09 mm filter. Additionally, when a separate Sn-0.4 mm filter, specific to 140 kV, is available, it contributes an additional 9% reduction in variance in water and Ca decomposition.

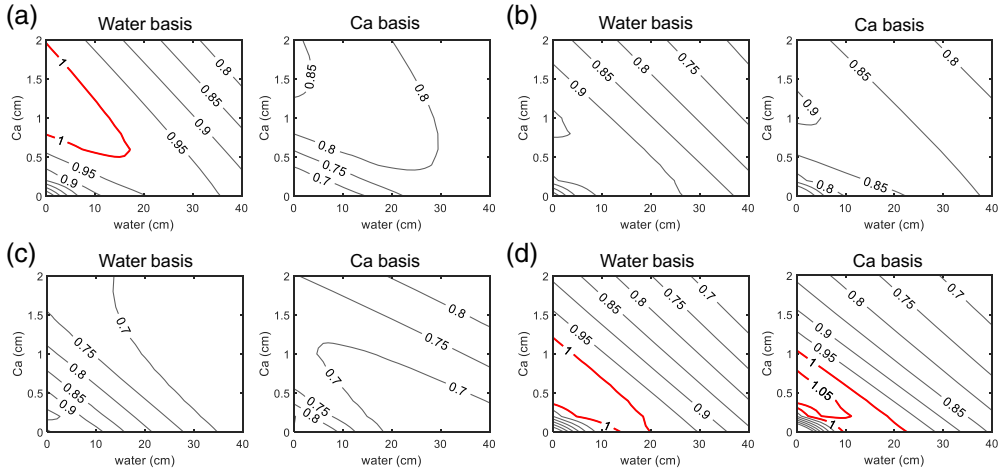

Fig. 5 CRLB ratio between fast kV switching (80/140 kV) and single kV (120 kV), with different dose allocations and fixed filters. A ratio of <1 indicates better performance for fast kV switching, while a ratio >1 indicates worse performance (outlined in red). (a) 80/140 kV, 50%/50% dose; (b) 80/140 kV, 30%/70% dose; (c) (80/140) kV + Gd-0.09 mm, 40%/60% dose; and (d) (80/140) kV + Sn-0.07 mm, 50/50% dose.

Table 2 Noise performance of various source settings (Si-60 mm detector response).

				Mean CRLB ratio				
Index	Source setting	Dose allocation (%)	mAs	Water	Ca	40 keV	60 keV	70 keV
1	120	100	1.00	1	1	1	1	1
2	120 + Gd-0.09 mm	100	1.74	0.8425	0.9375	1.0128	1.0983	0.9351
3	120 + Sn-0.07 mm	100	1.45	0.9881	1.1999	1.3370	1.1092	0.8566
4	80/140	30/70	0.95/0.47	0.8581	0.8527	0.8675	1.0083	1.0129
5	(80/140) + Gd-0.09 mm	40/60	3.56/0.65	0.7285	0.7192	0.7497	1.0283	1.0211
6	(80/140) + Sn-0.07 mm	50/50	4.21/0.46	0.8929	0.8715	0.8698	0.9240	0.9911
7	80/(140 Sn-0.4 mm)	60/40	1.90/0.90	0.6356	0.6294	0.6798	1.0081	0.9847

Figure 6 visualizes the results in Table 2, along with a full range of VMI energies and basis materials, to show the influences of source settings onto basis images and VMIs. For the CRLB results, the horizontal axis refers to VMIs at different energies. We place calcium and water material basis images at the two extremes, since low- and high-energy VMIs converge to these in the limit, respectively. Figure 6 also shows the spectra used (without filter), where the energies are aligned with the VMI energies to demonstrate the impact of real photons on VMI noise.

Although fast kV switching reduced the noise in basis images (water-Ca decomposition) and also reduced noise for the VMI at 40 keV, it slightly increased the noise at 60, 70, and 80 keV due to the occurrence of fewer real photons at these energies. Since VMIs generated close to the mean spectral energy exhibit the highest absolute image contrast-to-noise ratio (versus VMIs synthesized at other energies), this small relative deficit is unlikely to have a significant impact on clinical task performance.

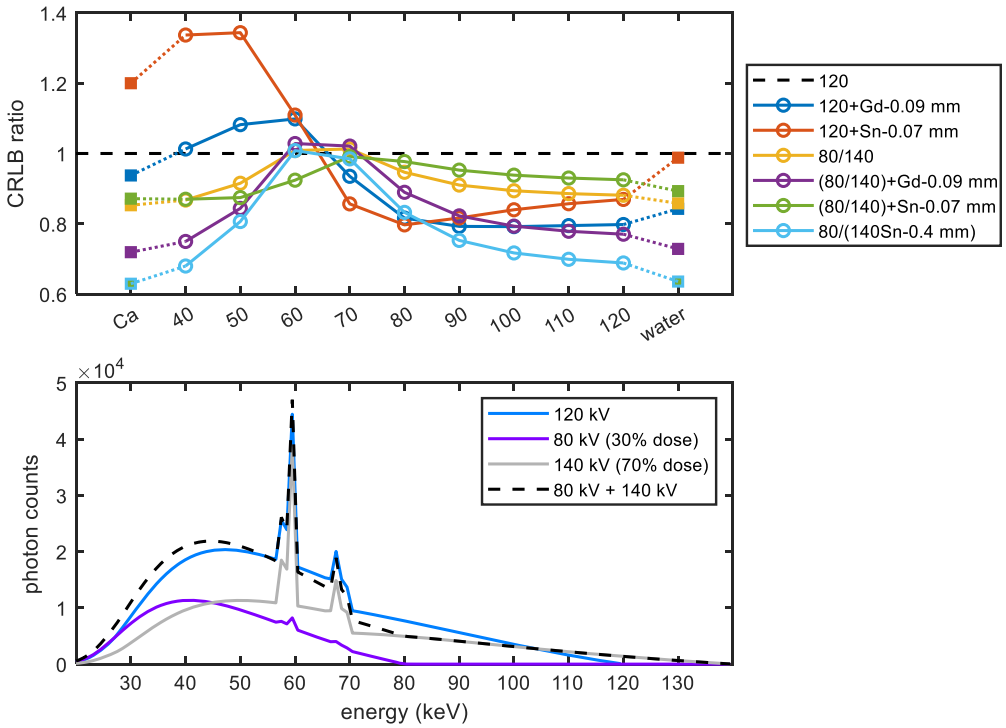

Fig. 6 Mean CRLB ratios of various source settings, along with the spectra without filters.

Table 3 Mean CRLB ratios of different detector designs for (80/140) + Gd-0.09 mm.

	Mean CRLB ratio				
detector	Water	Ca	40 keV	60 keV	70 keV
Si-30 mm	0.7467	0.7234	0.7450	1.0339	1.0220
Si-60 mm	0.7285	0.7192	0.7497	1.0283	1.0211
CdTe-1.6 mm	0.6030	0.5837	0.5950	0.9041	1.1073
CdTe-3 mm	0.6800	0.6651	0.6849	0.9904	1.1024

Adding a fixed Gd filter to fast kV switching can lower the noise in calcium and water tasks due to the enhanced spectral separation it imparts. However, this was achieved at the expense of slightly increased noise for the VMI at 60 keV. The Gd filter removes many photons in the middle of the spectrum due to the K-edge at 50.2 keV (Fig. 2), leading to increased noise for the VMIs at 50 and 60 keV. A fixed Sn-0.07 mm filter removes lower energy photons that are important for decomposing materials with higher photoelectric content (Ca), as well as for forming VMIs at lower keV values, leading to the degradation in those tasks while the inclusion of a separate Sn-0.4 mm filter for the 140 kV setting generally results in improved water-Ca decomposition and VMIs due to the improved spectral separation.

3.3 Other Detector Responses

To examine the generalizability of material decomposition with fast kV switching, we carried out similar simulation tests under other realistic detector responses including Si-30 mm, CdTe-1.6 mm, and CdTe-3 mm detectors. The mean CRLB ratios between fast kV switching (80/140 kV) with Gd filter and single kV (120 kV) are listed in Table 3. Noise reduction with fast kV switching can be found in basis material decomposition for all four detector responses; all of the mean CRLB ratios are substantially below 1. Also, CdTe detectors benefit more from fast kV switching because spectral tailing in the range of detected primary photons (>30 keV) is much more severe than for Si. (Si spectral tailing is largely limited to energies under 20 keV,[31] and these counts do not thus distort the parts of the spectrum that contain the information used in material basis decomposition). VMIs generally benefit, although noise increases slightly for Si at 60 keV and for CdTe at 70 keV.

3.4 Simulated Phantom Study

For the image domain analysis, we simulated a CT scan of an anthropomorphic head phantom[47] with the realistic Si-60 mm detector response first. Water and Ca basis images were reconstructed from material decomposition sinograms based on the analytical MLE. These images appear in Fig. 7, including the ground truth, single kV scan (120 kV), and fast kV switching using 80/140 kV with/without additional filters (Sn or Gd). The brain region used in the noise calculation for all the material images is highlighted in green in the ground-truth water image. Noise in term of SD from different source spectra in brain ROI is labeled for different source configurations.

We observe visibly reduced noise in the water basis image obtained with 80/140 kV and Gd filter compared to 120 kV. Overall trends in the image-domain noise are consistent with the projection-domain CRLB, again finding the most marked noise reduction for fast kV switching (+Gd filter).

Some penalty is observed in fast kV switching with Sn filter compared with 120 kV, whereas the CRLB results in Table 2 predict an overall noise reduction. This can be explained by the phantom size. The head phantom used in the study has a diameter of 15 to 20 cm, mostly comprised of water, which falls into the red region in Fig. 5(d).

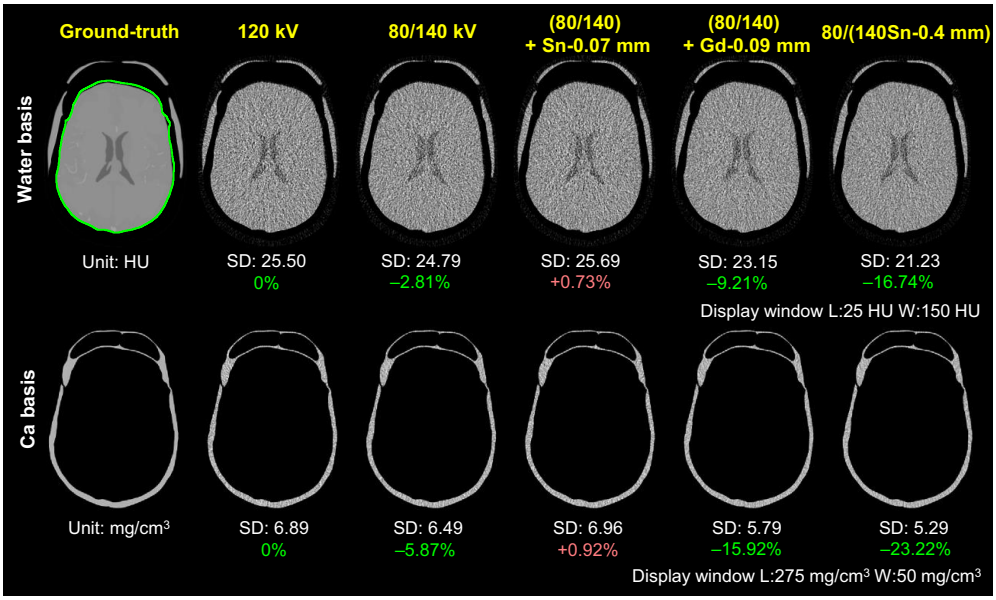

Fig. 7 Material decomposition images from different source spectra using Si-60 mm detector. (top) Water images and (bottom) Ca images. Noise in term of SD from different source spectra in brain ROI is labeled.

Table 4 Mean SD ratios in head phantom with different detector designs for (80/140) + Gd-0.09 mm.

	Mean SD ratio				
Detector	Water	Ca	40 keV	60 keV	70 keV
Si-30 mm	0.9185	0.8508	0.8284	1.0255	1.0083
Si-60 mm	0.9079	0.8408	0.8252	1.0243	1.0085
CdTe-1.6 mm	0.8162	0.7532	0.7343	1.0281	1.0383
CdTe-3 mm	0.8759	0.8087	0.7909	1.0420	1.0500

In Table 4, we present SD ratios between (80/140) + Gd and the 120 kV scan for all four detector responses. These ratios exhibit a consistent trend that aligns with the CRLB analysis findings in Table 3.

3.5 Three-Material Decomposition

K-edge imaging is one of the most important potential applications for PCDs. When a high-Z element with a K-edge is imaged, a third basis function should be added in the material decomposition model, leading to three-material decomposition.

3.5.1 *CRLB analysis in projection domain*

In addition to the range of water and calcium thicknesses, we included 1.0 cm of iodine with a concentration of 5 mg/mL, which is in the clinically relevant range,[36] and conducted a similar CRLB analysis. Figure 8 shows the CRLB ratio between fast kV switching (80/140 kV) and single kV (120 kV) for the water, calcium, and iodine bases for a range of water and calcium thicknesses. We find near-universal improvement in all basis materials, with an average variance reduction of 36.0%, 41.1%, and 41.2% for water, calcium, and iodine, respectively.

Compared with the CRLB ratios in two-material decomposition, the noise reduction in three-material decomposition is even greater with fast kV switching, which suggests that more

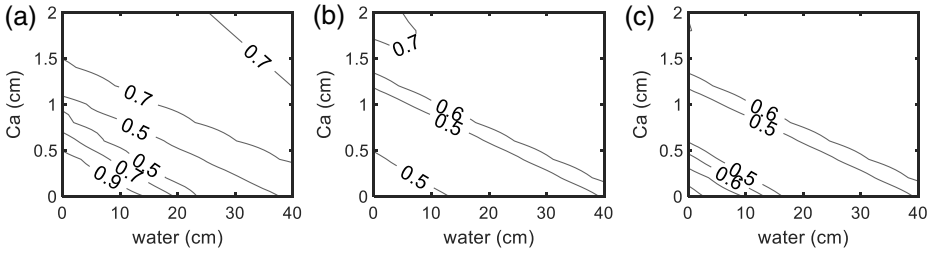

Fig. 8 CRLB analysis for three basis material decomposition using Si-60 mm response model. The CRLB ratios between fast kV switching (80/140 kV) and single kV (120 kV) are shown for water, Ca, and I bases, for a range of object sizes. (a) Water basis, (b) Ca basis, and (c) I basis.

challenging spectral tasks benefit more from the increased spectral information obtained from fast kV switching.

3.5.2 *Phantom study in image domain*

The phantom study was extended to include contrast-enhanced vessels, with a concentration of 5 mg/mL iodine, and three-material decomposition. Representative basis material images are shown in Fig. 9 for water, calcium, and iodine. Three-material decomposition with iodine as the third material can be quite noisy because identification of the iodine K-edge at 33.2 keV is challenging considering the presence of spectral tails (due to Compton scatter, K-escape fluorescence, and charge sharing) in nonideal detector response functions, as well as the limited number of photon counts in the low-energy range. To ensure a fair comparison, no denoising was applied here, although image quality can be substantially improved with denoising methods. Instead, we used a higher fluence of 4×10^7 photons/mm^2 per view in Fig. 9 for water, calcium, and iodine basis images. We acknowledge that the dose exceeds realistic clinical usage and is used solely in the simulation to better illustrate the relative differences. The noise reduction from 80/140 to 120 kV in terms of SD is 7.6%, 26.2%, and 25.8% for water, calcium, and iodine, respectively. These reductions correspond to a decrease in variance of 14.6% for water, 45.6% for calcium, and 45.0% for iodine, which is consistent with the CRLB analysis in Fig. 8.

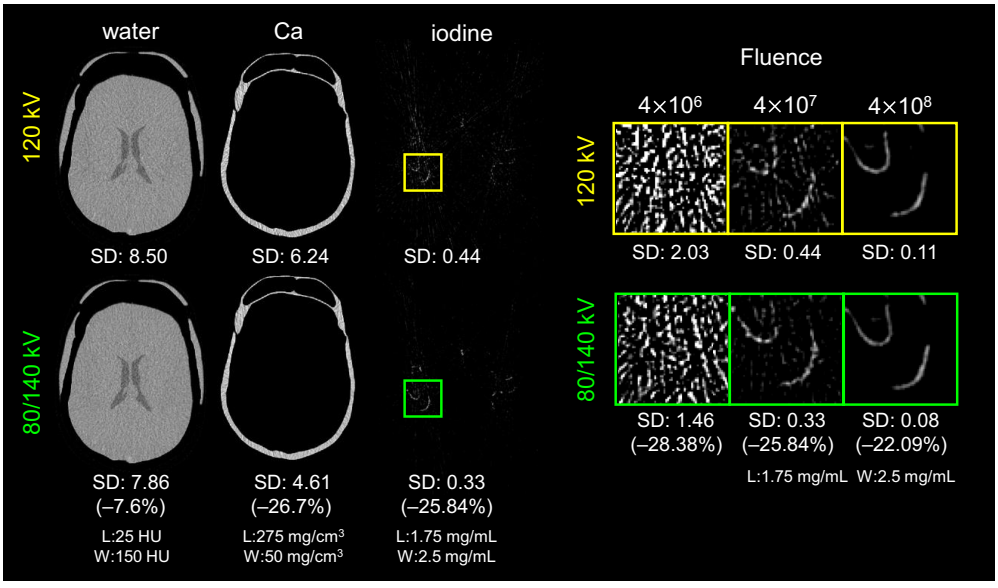

Fig. 9 Reconstructed images in three-material decomposition using Si-60 mm response model. Incident fluence for the illustration on the left is 4×10^7 photons/mm^2 per view. The right figure shows iodine images at various fluence levels in the selected ROI.

The right figure in Fig. 9 shows iodine images at various fluence levels in the selected ROI, which demonstrates that the reduction of noise with fast kV switching is robust and consistent across fluence levels as the fast kV switching noise is always less than the single kV scan.

4 Discussion

Our study focused on the potential of spectral optimization in PCCT systems to reduce noise in material decomposition tasks by applying fast kV switching techniques with or without an additional filter.

In two-basis material decomposition, we found that thicker areas benefit from higher kV levels for single kV scans, as expected. Fast kV switching requires proper dose allocation and filtration to outperform single-kV scans, such as with a fixed Gd-0.09 mm filter that outperformed single-kV scans nearly globally with a minor penalty for VMIs around 60 keV. The Sn filter is most beneficial when applied to the high kV only. For example, this could be achieved via synchronized fast switching of the filter (which is mechanically difficult to do) or with sequential scans or a dual-source system. Although dual-source PCD systems have an angular offset between the two sources, image-domain decomposition can be done, and using different source spectra [e.g., 80/(140 Sn-0.4 mm)] has been shown to be beneficial for two-material[30] and multicontrast imaging.[48] Three-basis material decomposition with a K-edge material (i.e., iodine) can be improved substantially using fast kV switching. Adding fixed filters, including Gd and Sn, are not helpful in three-material decomposition when iodine is the third K-edge material. Our results showed amplified noise in the basis material images with the addition of fixed filters. Although iodine benefits from the low-energy photons in the 80 kV spectrum of the fast kV switching pair, additional filters reduce the photons around the K-edge at 33.2 keV, leading to worse performance. We used iodine as the representative K-edge contrast material in this study, and our method can be easily extended to analyze other K-edge materials, such as Gd.

In this study, a configuration of eight energy bins was used, which is not common in contemporary CdTe detectors. We also evaluated fast kV switching with fewer energy bins, such as four energy bins, and found a slightly greater reduction in CRLB than that for eight energy bins for all the aforementioned detector responses. Future work could more thoroughly assess the optimal number of energy bins when combined with fast kV switching or dual spectra.

One limitation of our work was the use of the detectors' primary responses, without modeling object scatter, crosstalk (from Compton scatter and charge sharing), or pulse pileup. Since all of these factors degrade PCD spectral resolution, the improvements observed in this simulation study likely underestimate the actual benefits of optimal filtration and fast kV switching, but this needs to be verified and quantified. In photon counting systems, detector scatter, charge sharing, K-fluorescence, pileup, number of energy bins, energy thresholds, object size, object shape, object scatter, and bowtie filter design interact in complex ways. Our study used an idealized concept of fast kV switching and does not address the larger system-level issues that affect the practicality and clinical utility of spectral optimization methods.

5 Conclusions

In this work, we demonstrated the potential benefits of spectral optimization for reducing noise in material decomposition in PCCT systems. In addition to single-kV scan analysis, we specifically focused on the implementation of fast kV switching and filters to achieve noise reduction at equal dose levels. Our study covered two-material decomposition and three-material decomposition in both the projection and image domains. Fast kV switching with proper dose allocation and filtration consistently reduces the noise for both scenarios. In our future analysis and simulations, we plan to incorporate realistic scatter, crosstalk, pileup, and system effects and to validate our simulation findings with experimental data.

Disclosures

Debashish Pal, Zhye Yin, and Jonathan Maltz are/were employees of GE HealthCare. Norbert Pelc is a consultant for GE HealthCare.

Code and Data Availability

The data underlying this article will be shared on reasonable request to the corresponding author.

Acknowledgments

This work was supported by GE HealthCare.

References

1. R. E. Alvarez and A. Macovski, "Energy-selective reconstructions in X-ray computerised tomography," *Phys. Med. Biol.* **21**(5), 733 (1976).
2. T. R. Johnson et al., "Material differentiation by dual energy CT: initial experience," *Eur. Radiology* **17**(6), 1510–1517 (2007).
3. D. Zhang, X. Li, and B. Liu, "Objective characterization of GE discovery CT750 HD scanner: gemstone spectral imaging mode," *Med. Phys.* **38**(3), 1178–1188 (2011).
4. T. P. Szczykutowicz and G. H. Chen, "Dual energy CT using slow kVp switching acquisition and prior image constrained compressed sensing," *Phys. Med. Biol.* **55**(21), 6411 (2010).
5. N. Rassouli et al., "Detector-based spectral CT with a novel dual-layer technology: principles and applications," *Insights Imaging* **8**(6), 589–598 (2017).
6. R. Bhayana, A. Parakh, and A. Kambadakone, "Material decomposition with dual-and multi-energy computed tomography," *MRS Commun.* **10**(4), 558–565 (2020).
7. P. D. Lourenco et al., "Dual-energy CT iodine mapping and 40-keV monoenergetic applications in the diagnosis of acute bowel ischemia," *Am. J. Roentgenol.* **211**(3), 564–570 (2018).
8. E. K. Weidman et al., "Dual-energy CT angiography for detection of pulmonary emboli: incremental benefit of iodine maps," *Radiology* **289**(2), 546–553 (2018).
9. M. J. Connolly et al., "Diagnostic accuracy of virtual non-contrast enhanced dual-energy CT for diagnosis of adrenal adenoma: a systematic review and meta-analysis," *Eur. Radiol.* **27**, 4324–4335 (2017).
10. P. P. Zhang, H. H. Choi, and M. A. Ohliger, "Detection of fatty liver using virtual non-contrast dual-energy CT," *Abdom. Radiol.* **47**(6), 2046–2056 (2022).
11. C. Phan et al., "Differentiation of hemorrhage from iodinated contrast in different intracranial compartments using dual-energy head CT," *Am. J. Neuroradiol.* **33**(6), 1088–1094 (2012).
12. M. Tijssen et al., "The role of dual energy CT in differentiating between brain haemorrhage and contrast medium after mechanical revascularisation in acute ischaemic stroke," *Eur. Radiol.* **24**, 834–840 (2014).
13. J. L. Nute et al., "Dual-energy computed tomography for the characterization of intracranial hemorrhage and calcification: a systematic approach in a phantom system," *Investig. Radiol.* **52**(1), 30–41 (2017).
14. D. Marin et al., "Characterization of small focal renal lesions: diagnostic accuracy with single-phase contrast-enhanced dual-energy CT with material attenuation analysis compared with conventional attenuation measurements," *Radiology* **284**(3), 737–747 (2017).
15. K. Matsui et al., "Analysis of coronary arterial calcification components with coronary CT angiography using single-source dual-energy CT with fast tube voltage switching," *Int. J. Cardiovasc. Imaging* **31**(3), 639–647 (2015).
16. K. Taguchi and J. S. Iwanczyk, "Vision 20/20: single photon counting x-ray detectors in medical imaging," *Med. Phys.* **40**(10), 100901 (2013).
17. R. Gutjahr et al., "Human imaging with photon-counting-based CT at clinical dose levels: contrast-to-noise ratio and cadaver studies," *Investig. Radiol.* **51**(7), 421 (2016).
18. S. Leng et al., "A high-resolution imaging technique using a whole-body, research photon counting detector CT system," *Proc. SPIE* **9783**, 97831I (2016).
19. K. Rajendran et al., "Ultra-high resolution photon-counting detector CT reconstruction using spectral prior image constrained compressed-sensing (UHR-SPICCS)," *Proc. SPIE* **10573**, 1057318 (2018).
20. S. Leng et al., "Photon-counting detector CT: system design and clinical applications of an emerging technology," *Radiographics* **39**(3), 729–743 (2019).
21. J. R. Rajagopal et al., "Comparison of low dose performance of photon-counting and energy integrating CT," *Acad. Radiol.* **28**(12), 1754–1760 (2021).
22. T. Flohr et al., "Photon-counting CT review," *Phys. Med.* **79**, 126–136 (2020).
23. M. Danielsson, M. Persson, and M. Sjölin, "Photon-counting X-ray detectors for CT," *Phys. Med. Biol.* **66**(3), 03TR01 (2021).
24. A. Primak et al., "Improved dual-energy material discrimination for dual-source CT by means of additional spectral filtration," *Med. Phys.* **36**(4), 1359–1369 (2009).
25. S. Faby et al., "Performance of today's dual energy CT and future multi energy CT in virtual non-contrast imaging and in iodine quantification: a simulation study," *Med. Phys.* **42**(7), 4349–4366 (2015).
26. Y. Yao, A. S. Wang, and N. J. Pelc, "Efficacy of fixed filtration for rapid kVp-switching dual energy x-ray systems," *Med. Phys.* **41**(3), 031914 (2014).

27. P. M. Shikhaliev, "Photon counting spectral CT: improved material decomposition with K-edge-filtered X-rays," *Phys. Med. Biol.* **57**(6), 1595 (2012).
28. H. Chen et al., "Optimization of beam quality for photon-counting spectral computed tomography in head imaging: simulation study," *J. Med. Imaging* **2**(4), 043504 (2015).
29. H. Chen, M. Danielsson, and C. Xu, "Size-dependent scanning parameters (kVp and mAs) for photon-counting spectral CT system in pediatric imaging: simulation study," *Phys. Med. Biol.* **61**(11), 4105 (2016).
30. A. Tao et al., "Dual-source photon counting detector CT with a tin filter: a phantom study on iodine quantification performance," *Phys. Med. Biol.* **64**(11), 115019 (2019).
31. M. Persson, A. Wang, and N. J. Pelc, "Detective quantum efficiency of photon-counting CdTe and Si detectors for computed tomography: a simulation study," *J. Med. Imaging* **7**(4), 043501 (2020).
32. S. Wang et al., "Fast kV switching for improved material decomposition with photon counting X-ray detectors," *Proc. SPIE* **12031**, 120310F (2022).
33. E. Roessl and C. Herrmann, "Cramér–Rao lower bound of basis image noise in multiple-energy X-ray imaging," *Phys. Med. Biol.* **54**(5), 1307 (2009).
34. B. De Man et al., "CatSim: a new computer assisted tomography simulation environment," *Proc. SPIE* **6510**, 65102G (2007).
35. S. Slavic and M. Danielsson, "Dual-energy: the GE approach," in *Spectral Imaging*, H. Alkadhi et al., Eds., pp. 45–62, Springer (2022).
36. F. Grönberg et al., "Feasibility of unconstrained three-material decomposition: imaging an excised human heart using a prototype silicon photon-counting CT detector," *Eur. Radiol.* **30**(11), 5904–5912 (2020).
37. Y. Yang et al., "Empirical optimization of energy bin weights for compressing measurements with realistic photon counting X-ray detectors," *Med. Phys.* **51**, 224–238 (2024)
38. C. Ullberg et al., "Measurements on a novel 4-side buttable photon counting ASIC with integrating charge sharing correction," *Proc. SPIE* **12031**, 120310D (2022).
39. S. Wang et al., "Fast Monte Carlo simulation of non-isotropic X-ray source for CT dose calculation," in *Medical Physics*, AAPM Annual Meeting, Vol. 48, Wiley, Hoboken, New Jersey (2021).
40. A. Badal and A. Badano, "Accelerating Monte Carlo simulations of photon transport in a voxelized geometry using a massively parallel graphics processing unit," *Med. Phys.* **36**(11), 4878–4880 (2009).
41. S. Sudarski et al., "Optimization of keV-settings in abdominal and lower extremity dual-source dual-energy CT angiography determined with virtual monoenergetic imaging," *Eur. J. Radiol.* **82**(10), e574–e581 (2013).
42. J. L. Wichmann et al., "Virtual monoenergetic dual-energy computed tomography: optimization of kiloelectron volt settings in head and neck cancer," *Investig. Radiol.* **49**(11), 735–741 (2014).
43. A. Meier et al., "Advanced virtual monoenergetic images: improving the contrast of dual-energy CT pulmonary angiography," *Clin. Radiol.* **70**(11), 1244–1251 (2015).
44. D. Schneider et al., "Optimization of kiloelectron volt settings in cerebral and cervical dual-energy CT angiography determined with virtual monoenergetic imaging," *Acad. Radiol.* **21**(4), 431–436 (2014).
45. M. H. Albrecht et al., "Advanced image-based virtual monoenergetic dual-energy CT angiography of the abdomen: optimization of kiloelectron volt settings to improve image contrast," *Eur. Radiol.* **26**(6), 1863–1870 (2016).
46. K. E. Darras et al., "Virtual monoenergetic reconstruction of contrast-enhanced dual energy CT at 70 keV maximizes mural enhancement in acute small bowel obstruction," *Eur. J. Radiol.* **85**(5), 950–956 (2016).
47. S. E. Divel et al., "Development of a realistic, dynamic digital brain phantom for CT perfusion validation," *Proc. SPIE* **9783**, 97830Y (2016).
48. S. Tao et al., "Feasibility of multi-contrast imaging on dual-source photon counting detector (PCD) CT: an initial phantom study," *Med. Phys.* **46**(9), 4105–4115 (2019).

Sen Wang is a postdoctoral fellow in the Wang Group of the Department of Radiology at Stanford University. He completed his BS and PhD degrees at the Department of Engineering Physics at Tsinghua University in 2014 and 2019, respectively. His research interests focus on technologies and methods for image processing, reconstruction, and recognition, especially in the medical field.

Biographies of the other authors are not available.